

# Droplet migration in a Hele–Shaw microchannel: Effect of the lubrication film on the droplet dynamics

Yue Ling,<sup>1</sup> Jose-Maria Fullana,<sup>1</sup> Stéphane Popinet,<sup>1</sup> and Christophe Josserand<sup>1</sup>

*Institut Jean Le Rond d'Alembert, Sorbonne Universités,  
UPMC Univ Paris 06, CNRS, UMR 7190, Paris, F-75005,  
France*

Droplet migration in a Hele–Shaw microchannel is a fundamental multiphase flow problem which is crucial to many microfluidics applications. We focus on the regime at low capillary number, where the droplet keeps a circular shape in the horizontal plane. Parametric studies are performed on the droplet horizontal radius and the capillary number, and particular attention is paid to the effect of the lubrication film on the droplet velocity. For droplets with an horizontal radius larger than half of the channel height, the droplet overfills the channel and a lubrication film is formed between the droplet and the wall. The lubrication film is shown to have a strong impact on the droplet migration velocity and the three-dimensional flow structure. The droplet velocity in the present simulation is shown to be lower than the average inflow velocity, in contrast with the Taylor–Saffman theory for Hele–Shaw flows, but in agreement with experimental measurements. Both the strong shear induced by the lubrication film and the three-dimensional flow structure contribute to the low mobility of the droplet. In this low-migration-velocity scenario, the interfacial flow on the droplet is truly three dimensional and much more complex than in the high-migration-velocity case (the Taylor–Saffman solution). As a result the Hele–Shaw equation, which is a depth-averaged 2D approximation, is not valid for this case and three-dimensional effects must be taken into account in the analysis.

## I. INTRODUCTION

Droplet-based microfluidics is a promising tool for performing biochemical or chemical assays or to observe liquid-liquid extraction<sup>1-3</sup>. Droplets are unit systems of controlled volume and content, within which mixing, reacting and/or transferring can be achieved. Therefore, a comprehensive understanding of droplet migration in confined microchannels is essential to many microfluidics applications. Rectangular confined channels with the width significantly larger than the height are commonly used in microfluidics devices. In such cases, the confinement of the droplet is only in the vertical direction and the droplet is exposed to a two-dimensional Poiseuille flow (as in a Hele–Shaw cell). The migration of the droplet is driven by the ambient fluid with an average inflow velocity  $U_f$  and a constant terminal migration velocity  $U_d$  will be reached.

The ratio between the horizontal radius of the droplet ( $R$ ) and half of the channel height ( $H$ ) has been shown to have a strong effect on the droplet migration velocity  $U_d$  in a microchannel. (Hereafter we simply refer to  $U_d$  as the droplet velocity since the transient process is not of interest in the present study.) In the limit of  $R/H \rightarrow 0$  (as the droplet is a point mass) the droplet at the centerline of the channel will move with the maximum fluid velocity ( $U_{f,max} = 1.5U_f$ ). As  $R$  increases the droplet is exposed to the parabolic fluid velocity profile with a decreasing velocity toward the top and bottom walls and the droplet slows down. Theoretical studies on the velocity of droplets much smaller than the channel height have been conducted by many, see for example, Nadim and Stone<sup>4</sup> and Hudson<sup>5</sup>. As  $R$  further increases to be comparable or even larger than  $H$ , the droplet overfills the channel and a thin lubrication film is formed between the droplet interface and the wall. In this case the droplet loses its roughly spherical geometry and becomes “pancake-like” as schematically shown in Fig. 1. (For convenience of discussion, the axis corresponding to the channel length, height, and width are defined as  $x$ ,  $y$ , and  $z$ , respectively, see Fig. 1.) Beyond the influence of the parabolic velocity profile, the lubrication film further decreases the droplet velocity. A dramatical decrease of the droplet velocity at about  $R/H \approx 1$  has been observed in the experiments by Roberts *et al.*<sup>6</sup>

In contrast with scenarios in which the droplet is much smaller than the channel height, the dynamics of droplets with large  $R/H$  (i.e. pancake droplets) are more complicated and less understood. This regime is the focus of the present study. In the classic paper of

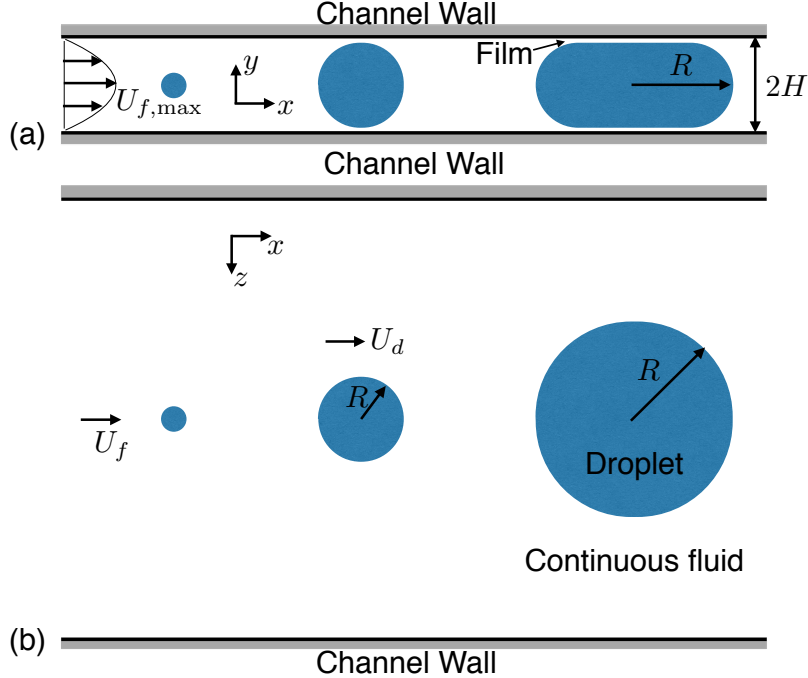


FIG. 1. Schematics of droplet migration in a Hele–Shaw microchannel for different droplet radius. (a) Side-view and (b) top-view.

Bretherton<sup>7</sup>, the dynamics and shape of a long bubble in a cylindrical channel, which is a two-dimensional axisymmetric analogue of the present problem, is studied analytically. The bubble length is considered to be much larger than the channel radius and as a result an annular film forms between the bubble and the wall. The film thickness  $h$  is governed by the balance between surface tension and viscous stresses. As the former tends to minimize the interface curvature and pushes the droplet interface closer to the wall, the latter tends to open up the gap between the droplet and the wall. Therefore the capillary number, which measures the relative importance of viscous stresses compared to surface tension, is a critical parameter to determine  $h$  and the droplet dynamics. Beyond the capillary number, the viscosity ratio between the droplet and the ambient fluid has also been shown to have a significant influence on the lubrication film thickness and the flow pattern<sup>8</sup>.

Predicting the bubble/droplet velocity  $U_d$  in the case of a 3D rectangular (Hele–Shaw) channel is more challenging. Early efforts on predicting velocity of a flat bubble/droplet in a Hele–Shaw cell go back to the pioneering work by Taylor and Saffman<sup>9</sup>. The Hele–Shaw equations are obtained by averaging the Stokes equations along the channel height (depth), and are thus a 2D representation of the depth-averaged velocity and pressure on the  $x$ - $z$

plane. One can then show that the bubble velocity  $U_d$  is always larger than the average inflow velocity  $U_f$ . When the horizontal cross-section of the bubble is strictly a circle, then  $U_d = 2U_f$ . When  $U_f < U_d < 2U_f$  or  $U_d > 2U_f$  the bubble horizontal cross-section is elliptical with shorter or longer axes in the direction of the flow. The surface tension was originally ignored, but it has been shown that the inclusion of surface tension does not significantly change the results<sup>10,11</sup>. However in the later experiments by Kopf-Sill and Homsy<sup>12</sup>, the measured bubble velocity is found to be very different from the Taylor–Saffman prediction. In particular, for near-circular bubbles at low capillary number,  $U_d$  is about  $0.2U_f$  which is an order of magnitude smaller than the predicted value  $2U_f$ . Saffman and Tanveer<sup>13</sup> investigated the possible mechanisms neglected in the original theory that may account for the large discrepancy with the experiments of Kopf-Sill and Homsy. They suggested that the low bubble velocity may be due to the excessive drag from the thin film, which may in turn be due to the existence of a moving contact line along the channel wall. However in the experiments of Kopf-Sill and Homsy, the ambient fluid always wetted the wall, which implies that the low mobility of the bubble was quite unlikely due to a moving contact line. Park *et al.*<sup>14</sup> suggested that the low bubble velocity observed in the experiments of Kopf-Sill and Homsy and the discrepancy with the Taylor–Saffman prediction could be due to surfactants and associated Marangoni effects. Surfactant transport on the droplet interface can indeed significantly increase the drag on the bubble. In their experiments (with parameters similar to those by Kopf-Sill and Homsy), the velocity of pure air bubbles in silicon oil is in reasonable agreement with the prediction of Taylor and Saffman, which suggests that the Taylor–Saffman theory is indeed valid in predicting the bubble velocity if the bubble interface is truly “stress-free” and the film introduces no excessive drag<sup>15</sup>. In the experiments of Park *et al.* water droplets were also considered. The migration velocity of pure water droplets, which were expected to move as fast as air bubbles since the influence of surfactants was excluded, was again much lower than expected, to an extent similar to the results of Kopf-Sill and Homsy. Park *et al.*<sup>14</sup> then explained that this low droplet velocity might be due to the fact that the “pure” water droplet in the experiment still contained some surfactants. However the droplet velocity varied little in their experiments when the surfactant concentration increased from 0 to 20%, and was always smaller than the average inflow velocity. Furthermore, as will be shown later, the present simulations with constant surface tension also produce low droplet velocities (smaller than  $U_f$ ). Therefore Marangoni

effects may not be the only reason for the low mobility of bubbles or droplets.

To investigate the droplet dynamics in a Hele–Shaw microchannel, a comprehensive understanding of the three-dimensional flow structure is crucial. Due to the small scale of microfluidics systems, experimental measurements of the details of the micro-scale flow structure are difficult. In typical experimental setups the horizontal shape and velocity of the droplet and the pressures and flow rates at the inlet and outlet of the channels can be measured. Recently Huerre *et al.*<sup>16</sup> presented quantitative optical measurements of lubrication film thicknesses as small as 20 nm. However it is very challenging to probe local values of velocity and pressure, and consequently the flow structure inside and outside of the droplet is hard to obtain. Furthermore, as the flow field is truly three-dimensional and complex, analytical approaches are very limited. Therefore 3D direct numerical simulations which provide a complete description of the flow field can shed light on the present problem. As the scales of microfluidics are much larger than the molecular scale the continuum mechanics approach is still valid. It has been shown that numerical approximations of the Navier-Stokes equations can represent flow physics in many microfluidics applications, such as droplets/bubbles migration and the breakup of droplets at T-junctions<sup>17–20</sup>.

Nevertheless 3D simulations of droplet migration in a microchannel are challenging as well. This is in particular true for droplets with large ratio  $R/H$  and small  $Ca$ . Since capillary effects are dominant the time step used in the temporal integration is controlled by the surface tension term in the momentum equation. For small capillary numbers the time step becomes very small and thus the number of steps for the terminal velocity of droplet to be reached is huge. In addition, at low capillary numbers the thickness of the lubrication film becomes very small (several orders of magnitude smaller than the channel height). For example for a channel height  $2H = 25\mu\text{m}$  the film thickness has been observed to be as small as 20 nm<sup>16</sup>. Since the mesh resolution and the time step restriction are dictated by the smallest length scale in the problem, the total number of cells and integration steps in 3D simulation are both very large. Three-dimensional simulation results of droplet/bubble in microchannels have not been reported until the very recent works by Hoang *et al.*<sup>20</sup> and Roberts *et al.*<sup>6</sup> However, as far as the authors are aware, no previous works have ever been reported for 3D simulations of droplet with a large  $R/H$  and with a lubrication film formed.

The goal of the present study is to investigate the droplet migration in a Hele–Shaw microchannel through 3D direct numerical simulations. The capillary number of the droplet

is considered to be small enough so that the horizontal shape of the droplet is near-circular according to the category of Kopf-Sill and Homsy<sup>12</sup>. Particular attention will be paid to the effects of the lubrication film on the droplet dynamics. A two-phase flow solver, Gerris<sup>21,22</sup>, is employed for the simulation. In the Gerris solver, the Volume-of-Fluid (VOF) method is used to resolve the interface between the two phases and an adaptive mesh is used to refine the mesh only in necessary regions, such as the interface, so that the computational cost can be reduced. The governing equations and the numerical methods are presented in section II. The simulation results will be shown in sections III and IV. We will first perform simulations of 2D droplets migrating in a microchannel with parameters similar to the 3D case for the purpose of validation, see III. The simulation results and discussions for the 3D droplet are then presented in section IV. Finally, we draw conclusions on the present study.

## II. GOVERNING EQUATIONS AND NUMERICAL METHODS

### A. Governing equations

The one-fluid approach is employed to resolve the two-phase flow, where the phases corresponding to the droplet and the ambient fluid are treated as one fluid with material properties that change abruptly across the interface. The incompressible, variable-density, Navier-Stokes equations with surface tension can be written as

$$\rho(\partial_t \mathbf{u} + \mathbf{u} \cdot \nabla \mathbf{u}) = -\nabla p + \nabla \cdot (2\mu \mathbf{D}) + \sigma \kappa \delta_s \mathbf{n}, \quad (1)$$

$$\nabla \cdot \mathbf{u} = 0, \quad (2)$$

where  $\rho$ ,  $\mu$ ,  $\mathbf{u}$ , and  $p$  represent density and viscosity, velocity and pressure, respectively. The deformation tensor is denoted by  $\mathbf{D}$  with components  $D_{ij} = (\partial_i u_j + \partial_j u_i)/2$ . The third term on the right hand side of Eq. (1) is a singular term, with a Dirac distribution function  $\delta_s$  localized on the interface, and it represents the surface tension force. The surface tension coefficient is  $\sigma$ , and  $\kappa$  and  $\mathbf{n}$  are the local curvature and unit normal of the interface.

The volume fraction  $C$  is introduced to distinguish the different phases, in particular  $C = 1$  in the computational cells with only the ambient fluid (respectively  $C = 0$  in the droplet), and its time evolution satisfies the advection equation

$$\partial_t C + \mathbf{u} \cdot \nabla C = 0. \quad (3)$$

The fluid density and viscosity are then defined by

$$\rho = C\rho_f + (1 - C)\rho_d, \quad (4)$$

$$\mu = C\mu_f + (1 - C)\mu_d. \quad (5)$$

where the subscripts  $f$  and  $d$  represent the ambient fluid and the droplet respectively.

## B. Numerical methods

The Navier-Stokes equations (Eqs. (1) and (2)) are solved by the open-source package Gerris<sup>21,22</sup>. In Gerris, a finite volume approach based on a projection method is employed. A staggered-in-time discretisation of the volume-fraction/density and pressure leads to a formally second-order accurate time discretisation. The interface between the different fluids are tracked and followed using a Volume-of-Fluid (VOF) method<sup>23,24</sup>. A quad/octree spatial discretisation is used, which gives a very important flexibility allowing dynamic grid refinement into user-defined regions<sup>21</sup>. Finally the height-function (HF) method is employed to calculate the local interface curvature, and a balanced-force surface tension discretization is employed<sup>22</sup>.

Both temporal and spatial schemes of integration are explicit. Therefore, numerical stability requires the time step for integration to satisfy the stability conditions corresponding to the advection, viscous, and surface tension terms, respectively<sup>24</sup>. Since the Reynolds and capillary numbers in the present problem are both very small, the time step restriction is dominated by the contribution from the surface tension force, *i.e.*

$$\Delta t \leq \sqrt{\frac{\rho\Delta^3}{\pi\sigma}} \quad (6)$$

where  $\Delta$  represents the cell size. For droplets with large  $R/H$ , the thickness of the lubrication film is the smallest scale in the problem and thus dictates the smallest cell size and the time step (according to Eq. (6)) to be used. The ratio of lubrication scale to channel height can be assumed to scale like  $Ca^\alpha$  (with  $\alpha = 2/3$  for 2D droplets) so that the total number of grid points (on a regular Cartesian grid) will scale like  $Ca^{-D\alpha}$  with  $D$  the dimension of the problem. If we assume that the terminal migration velocity is reached after a time of order  $\sqrt{\frac{\rho H^3}{\pi\sigma}}$  (the oscillation period of the drop), the total number of time steps will be of order  $Ca^{-3\alpha/2}$ . The total work (number of grid points times number of time steps) will

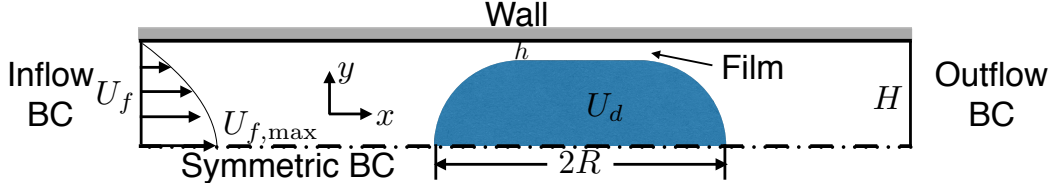


FIG. 2. Two-dimensional simulation setup for a droplet in a planar microchannel.

thus scale like  $Ca^{-(D+3/2)\alpha}$  i.e.  $\approx Ca^{-3}$  for a 3D problem. Given that capillary numbers for microfluidics applications can be as low as  $10^{-5}$ , we see that direct numerical simulations will be extremely expensive. The adaptive mesh refinement in Gerris allows to refine the mesh only in the lubrication film, which greatly decreases this cost, however this is still not sufficient to be able to reach such a low capillary number.

### III. 2D SIMULATIONS OF DROPLET MIGRATION IN A MICROCHANNEL

Before we present the 3D results, 2D simulations for a droplet moving in a microchannel are performed for validation purpose. The schematic of the simulation setup is shown in Fig. 2. The flow is symmetric in the  $y$  direction with regard to the axis  $y = 0$ , thus only the upper half of the channel is considered. The half-height of the channel is denoted by  $H$ . The inflow from the left boundary is a parabolic velocity profile with mean value  $U_f$  and maximum value  $U_{f,max} = 1.5U_f$ . An outflow boundary condition is applied at the right boundary of the domain; while the top boundary is taken as a no-slip wall. The length of the bubble is denoted by  $2R$ , and  $R/H = 2$ . As the droplet is constrained by the channel, a lubrication film is formed between the droplet and the wall. The channel length is  $L_x = 16H$ , which is long enough for the droplet to reach its terminal velocity  $U_d$  before being affected by the outflow boundary.

The physical properties of the ambient fluid and the droplet are listed in Table I, which are similar to the recent experiments by Roberts *et al.*<sup>6</sup> The Reynolds number based on the channel height and average inflow velocity,  $Re_f = \rho_f U_f H / \mu_f$ , is taken to be 1.35. The surface tension is varied from 0.0002 to 0.0159 N/m.

Bretherton<sup>7</sup> studied theoretically and experimentally the dynamics of a long bubble in a confined cylindrical channel. In the limit of small capillary number, *i.e.*,  $Ca = \mu_f U_d / \sigma \ll 1$ ,

TABLE I. Physical properties of the ambient fluid and the droplet in the present study. <sup>a</sup>

$\hat{\rho}_f$ (Kg/m <sup>3</sup> )	$\hat{\rho}_d$ (Kg/m <sup>3</sup> )	$\hat{\mu}_f$ (Pa s)	$\hat{\mu}_d$ (Pa s)	$\hat{H}$ ( $\mu\text{m}$ )	$\hat{U}_f$ (m/s)
750	1000	$7.4 \times 10^{-4}$	$10^{-3}$	50	0.0267

<sup>a</sup> Symbol with  $\hat{\cdot}$  denotes dimensional parameters.

it is shown that the ratio between the film thickness  $h$  and the half-height of the channel  $H$  scales as  $Ca^{2/3}$ , as does the ratio between the excess of droplet velocity compared to the mean inflow velocity of the ambient fluid:

$$\frac{h}{H} = \frac{(U_d - U_f)}{U_f} \sim Ca^{2/3} \quad (7)$$

the proportionality constant depends on the geometrical configuration (planar or cylindrical channels) and the viscosity ratio, although temperature and surfactants may also modify the surface tension. It can be shown that  $h/H$  is related to  $(U_d - U_f)/U_f$  through mass fluxes balance.

In the original work of Bretherton<sup>7</sup>, the viscosity of the fluid within the bubble is considered to be zero. An extension to droplets of arbitrary viscosity was given later by Hodges *et al.*<sup>8</sup> The theory for a slender droplet in a cylindrical channel is readily modified for a 2D droplet confined by two parallel plates like the present problem. The film thickness and the excess of droplet velocity for a 2D droplet in the limits of  $\mu_d \rightarrow 0$  (bubbles) and  $\mu_d \rightarrow \infty$  (very viscous droplets) are given by

$$\frac{h}{H} = \frac{U_d - U_f}{U_f} \sim 0.643 (3Ca)^{2/3}. \quad (8)$$

and

$$\frac{h}{H} = \frac{U_d - U_f}{U_f} \sim 0.51 (3Ca)^{2/3}, \quad (9)$$

respectively<sup>17</sup>. Similar scaling relations have also been derived for moving foams as well as bubble trains in micro-devices<sup>25</sup>.

The multi-scale nature of the problem can be seen through Eqs. (8) and (9). For a capillary number of  $10^{-4}$ ,  $h/H = 0.00288$  and therefore the length scales involved in the system span over three orders of magnitudes. This fact highlights the importance of the adaptive mesh refinement technique for the present study, which reduces the overall computational costs by refining the mesh only in the lubrication film and near the interface.

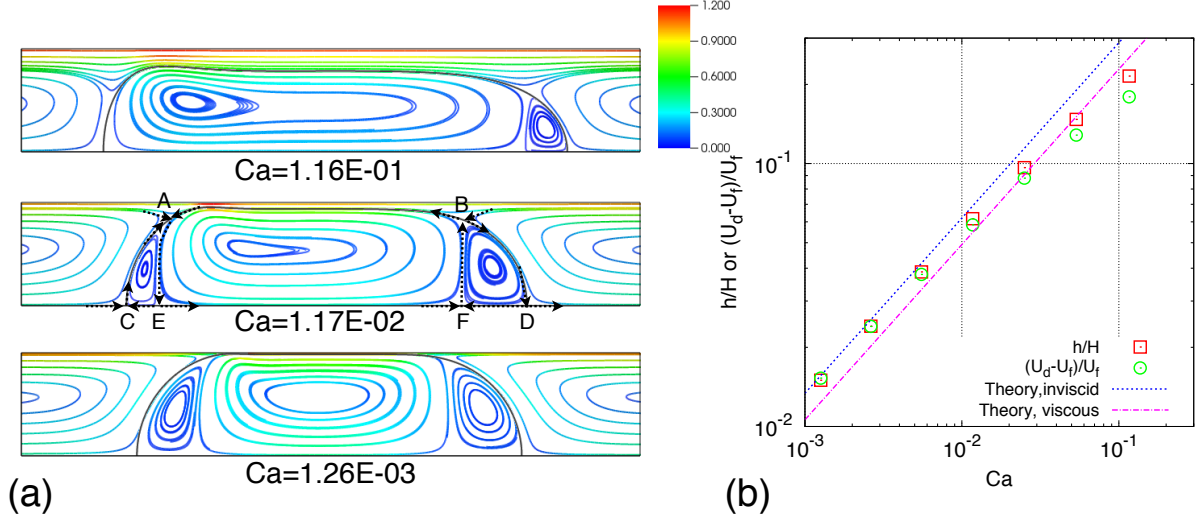


FIG. 3. (a) Droplet shape and the streamlines in the droplet reference frame. The color of the streamlines denotes the velocity magnitude in the droplet reference frame. (b) Relative droplet velocity and film thickness as functions of the capillary number.

The shapes of the droplets and the corresponding streamlines in the droplet reference frame are shown in Fig. 3(a) for different capillary numbers. The color of the streamlines denotes the velocity magnitude in the droplet reference frame. The droplet shape and flow pattern are in full agreement with the theory<sup>7,8</sup>. Under the effect of the viscous stress, the radius of curvature at the front of the droplet is smaller than that at the rear. A small bump is visible on the top-rear of the droplet. The four stagnation points on the droplet interface (A: top-rear; B: top-front; C: rear; D: front) and the other two inside the droplet (E: near the rear; F: near the front) are clearly seen. For small  $Ca$ , the major recirculation (A-E-F-B-A) is located at the center of the droplet, with two minor ones sitting on both sides (A-E-C-A and B-F-D-B). When  $Ca$  increases the major recirculation shifts toward the rear of the droplet and the two minor recirculation zones become smaller. When the capillary number reaches  $Ca = 0.116$  the stagnation points C and E get very close and the minor recirculation near the rear disappears.

Figure 3(b) shows a quantitative comparison between the numerical and the theoretical results for the droplet velocity and the film thickness. The excess of droplet velocity  $(U_d - U_f)/U_f$  and film thickness  $h/H$  are plotted as functions of the droplet capillary number  $Ca$  in log-log scale, for  $Ca$  varying from  $1.24 \times 10^{-3}$  to  $9.87 \times 10^{-2}$ . The droplet velocity in

the simulation is evaluated by a weighted-integral over all the cells occupied by the droplet fluid, *i.e.*,  $U_d = \int_S u (1 - C) dS / \int_S (1 - C) dS$ . It is seen that the simulation results match the theoretical results quite well. For large Ca the simulation results are slightly lower than the theoretical prediction. Therefore the asymptotic theory of Bretherton<sup>7</sup> seems to provide reasonable predictions of the droplet dynamics up to about Ca = 0.1. This observation is consistent with the previous studies by Afkhami *et al.*<sup>17</sup>

#### IV. 3D SIMULATIONS OF DROPLET MIGRATION IN A HELE–SHAW MICROCHANNEL

In this section we present the 3D simulation results of droplet migration in a Hele–Shaw microchannel. The physical properties of the ambient fluid and the droplet are identical to those of the previous 2D simulations, but the droplet is 3D and the cross-section in the  $x$ - $z$  plane is close to a circle.

##### A. Simulation setup

The computational domain for a 3D droplet migration in a Hele–Shaw microchannel is shown in Fig. 4. It is assumed that the droplet motion and the corresponding flow is symmetrical in the  $y$  and  $z$  directions, with respect to the planes  $y = 0$  and  $z = 0$ , respectively. Therefore, only a quarter of the overall domain is actually computed. Taking the half-height of the channel  $H$  as the typical length scale, the length, height, and width of the computational domain are taken as  $L_x = 16H$ ,  $L_y = H$ , and  $L_z = 8H$ , respectively.

An inflow boundary condition is imposed on the left of the domain with a parabolic velocity profile. Correspondingly an outflow boundary condition is used on the right. The top of the domain is taken to be no-slip wall with a velocity  $U_w$  in the opposite direction with respect to the flow. Therefore the simulation is indeed conducted in a moving reference frame with a mean inflow velocity of  $U_f - U_w$ . The purpose of using a moving reference frame is to keep the droplet near the center of the domain and to avoid the influence of the boundaries. Ideally the terminal droplet velocity in the lab reference frame  $U_d$  should be used for  $U_w$ , but since  $U_d$  is unknown a priori, an initial guess of  $U_d$  is used for  $U_w$ . Nevertheless as long as the droplet does not get too close to the inflow and outflow boundaries, the specific

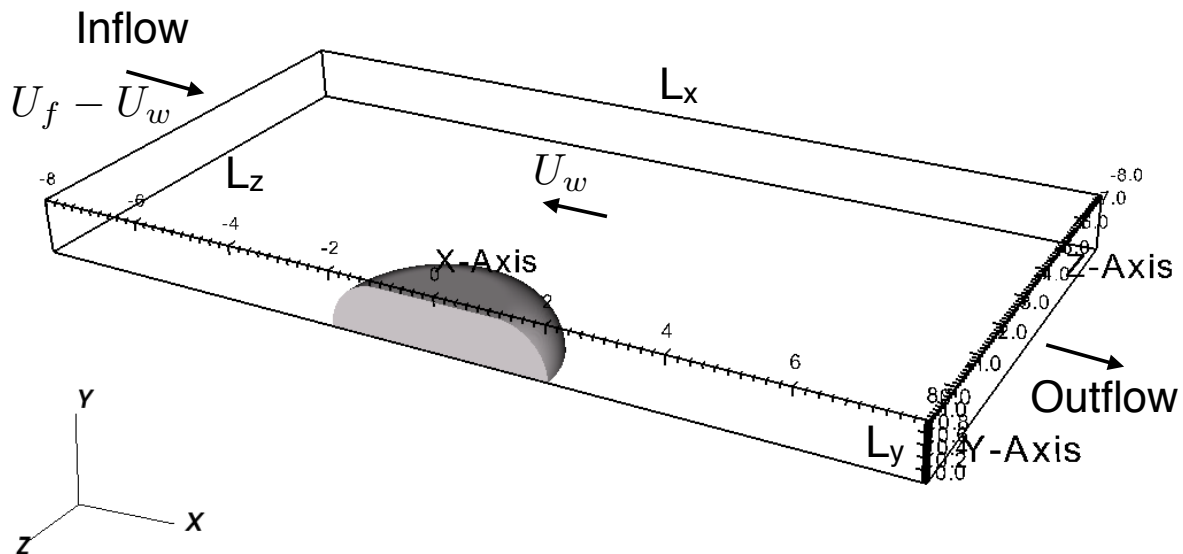


FIG. 4. Three-dimensional simulation setup for a droplet in a Hele–Shaw microchannel.

value of  $U_w$  is immaterial to the simulation results. Finally the other boundaries are set to symmetric boundary conditions.

The droplet is taken to be initially stationary in the simulation frame. Driven by the ambient fluid flow the droplet approaches the terminal droplet velocity as time evolves. The initial shape of droplets with  $R/H < 1$  is taken to be a sphere with radius  $R$ . For  $R/H \gtrsim 1$  the cross-section at  $y = 0$  is a circle with radius  $R_0$ . The top of the droplet is initially flat with a constant distance of  $0.1H$  to the top wall. The “edge” of the droplet is formed by a quarter of a circle of radius of  $0.9H$  rotated with respect to the  $y$  axis, see Fig. 4. Similar to the droplet velocity, the droplet will evolve to the final shape for which the surface tension and viscous forces at the interface are in perfect balance. The final value of  $R$ , calculated based on the horizontal cross-section area  $S_{y=0}$  (at the plane  $y = 0$ ) as  $R = \sqrt{2S_{y=0}/\pi}$ , is slightly different from its initial value  $R_0$ . Due to the initial configuration we impose, the difference between  $R$  and  $R_0$  is generally small. (Therefore from here on we do not distinguish  $R_0$  and  $R$  unless otherwise indicated.) Similar to the velocity of the top wall, the specific details of the initial shape of the droplet are not relevant to the final results as long as the terminal droplet velocity and shape are reached.

An adaptive mesh is used to discretize the spatial domain. The finest cell size used is  $\Delta_{\min} = H/128$ . The mesh is refined at the interface based on the gradient of the volume

TABLE II. Key dimensionless parameters in 3D simulations.

$r = \rho_f/\rho_d$	$m = \mu_f/\mu_d$	$\text{Re}_f = \rho_f U_f H/\mu_f$	$R/H$	$\text{Ca}_f = \mu_f U_f/\sigma$
0.75	0.74	1.35	0.5 to 2	$6.17 \times 10^{-3}$ to $9.87 \times 10^{-2}$

fraction in each cell. Mesh refinement is also conducted using an a posteriori error estimate of all three velocity components as a cost function for adaptation. A mesh refinement study was performed in the 2D simulations, showing that  $\Delta_{\min}$  is sufficient for the range of capillary numbers considered in the present study.

The physical parameters are identical to the 2D simulation presented in section III (see Table I). Parametric studies are performed by varying the surface tension coefficient  $\sigma$  and the droplet radius  $R$ . Taking the ambient fluid density  $\rho_f$ , the half of the channel height  $H$ , and the mean inflow velocity  $U_f$  as characteristic scales, the unknown variables and physical parameters can be non-dimensionalized and the governing equations (Eqs. (1)–(3)) are solved in dimensionless form. The key dimensionless parameters of the present problem are given in Table II. As shown in the table, the ratio  $R/H$  and the capillary number based on the average inflow velocity  $\text{Ca}_f$  are chosen as the tuning parameters.

The capillary numbers in the 3D simulation are significantly larger than that in experiments by Roberts *et al.*<sup>6</sup>, in which  $\text{Ca}_{f,\text{Exp}} = 9.87 \times 10^{-4}$ . The smallest  $\text{Ca}_f$  considered here is about an order of magnitude larger than this experimental value. As illustrated in the previous 2D results, the lubrication film formed is very small for small capillary numbers. It is prohibitively difficult to simulate droplets with a larger  $R/H \gtrsim 1$  and a small  $\text{Ca}_f$  comparable to the experimental value with current computational resources. Nevertheless it is expected that as long as the thickness of the lubrication film does not reach the regime where van der Waals forces are important, the effect of the lubrication film on the droplet dynamics can still be captured with simulation results at larger  $\text{Ca}_f$ . At the end of this section an extensive discussion on the effect of surface tension will be given.

## B. Effect of droplet horizontal radius on droplet dynamics

The temporal evolution of the droplet velocity is shown in Fig. 5(a) for  $\text{Ca}_f = 9.87 \times 10^{-2}$  and  $R/H$  varying from 1 to 2. When  $R/H$  increases,  $U_d$  decreases and in contrast, the time it

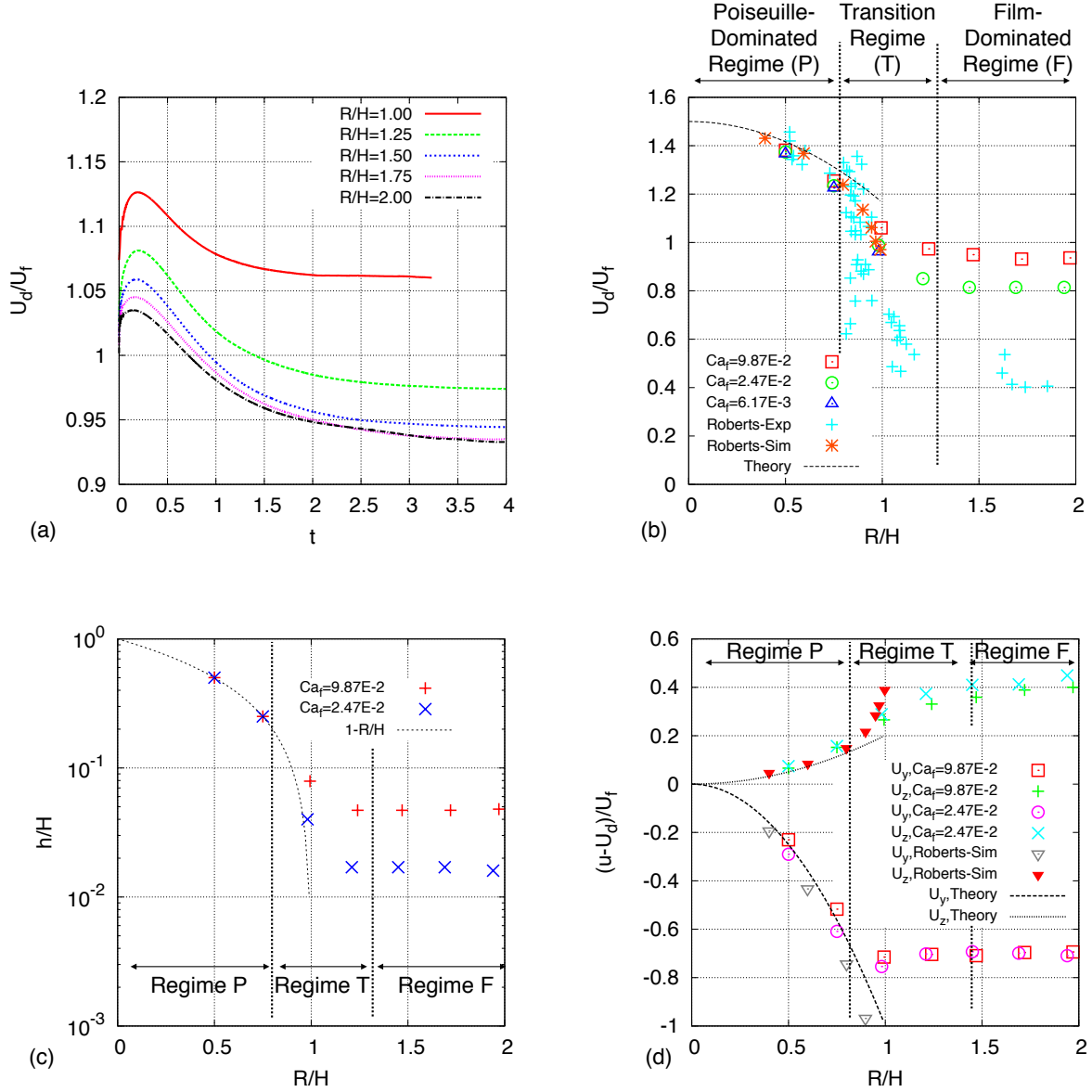


FIG. 5. (a) Temporal evolution of mean droplet velocity. (b) Terminal mean droplet velocity  $U_d$ , (c) thickness (height) of the gap (film) between the droplet interface and the top channel wall, denoted by  $h$ , and (d) relative  $u$ -velocities at the top and the side of the droplet ( $U_y$  and  $U_z$ ) as a function of the ratio between the droplet radius  $R$  and half of the channel height  $H$ . The experimental and theoretical results are shown for comparison<sup>4-6</sup>.

takes for the droplet to reach its terminal velocity increases (while identical initial conditions are imposed). From  $R/H = 1$  to  $1.25$ ,  $U_d$  decreases significantly (about 9%). The decrease of  $U_d$  with  $R/H$  becomes more gradual for larger  $R/H$ . It is seen that the difference between  $U_d$  for  $R/H = 1.75$  and  $R/H = 2$  becomes invisible as  $t > 2$ .

The simulation results of the droplet velocity as a function of  $R/H$  are shown in Fig. 5(b). The experimental and simulation results of Roberts *et al.*<sup>6</sup> and the theoretical results of Nadim and Stone<sup>4</sup> for small  $R/H$  are also shown for comparison. The present predictions of  $U_d$  are in good agreement with both the theoretical and experimental results for  $R/H < 1$ .

For  $R/H > 1$  the simulation results of  $U_d$  are larger than those measured in the experiment. The discrepancy is expected since smaller surface tension coefficients (or larger capillary numbers) are considered in the simulation. Nevertheless the simulation results capture well the trend of variation of  $U_d$  with  $R/H$ , *i.e.*, initially  $U_d$  decreases as a parabolic function, then decreases rapidly for  $0.75 \lesssim R/H \lesssim 1.25$  and at last reaches a plateau for  $R/H > 1.5$ . The trend of  $U_d$  variation with  $R/H$  is also consistent with the experimental observations. Furthermore it is observed that the plateau value of  $U_d$  for large  $R/H$  decreases with  $Ca_f$ , approaching toward the experimental value which corresponds to a much smaller  $Ca_f$ .

According to the numerical and experimental results, the variation of  $U_d$  with  $R/H$  can be divided into three different regimes: the Poiseuille-dominated regime, the transient regime and the film-dominated regime, which are schematically shown in Fig. 5. In each regime different mechanisms dominate the droplet migration in the Hele–Shaw microchannel.

- Poiseuille-dominated regime (Regime P),  $R/H \ll 1$ : When  $R/H \rightarrow 0$ , the droplet velocity is close to the maximum fluid velocity in the channel  $U_{f,max}/U_f = 1.5$ . When  $R/H$  increases,  $U_d$  decreases as the droplet is exposed to lower fluid velocity in the parabolic velocity profile. The deviation of  $U_d$  from  $U_{f,max}$  is a parabolic function of  $R/H$  as shown by Nadim and Stone<sup>4</sup>. In this regime the droplet velocity is dominated by the Poiseuille flow in the Hele–Shaw cell. As the gap between the droplet and the top wall is relatively large, its thickness is not affected by the wall. The droplet remains close to a sphere, so  $h/H$  closely follows  $1 - R/H$ .
- Transition regime (Regime T),  $R/H \approx 1$ : In this regime, the droplet just overfills the channel and the lubrication film just starts to form. The film thickness starts to deviate from  $1 - R/H$  and is now governed by the viscous stress and the surface tension. The film formation significantly influences the droplet velocity and a rapid decrease of  $U_d$  is clearly observed. A rough estimate of the film area for  $R/H > 1$  can be given as  $A_{Film}/S_{y=0} \approx (1 - H/R)^2$  and it can be shown that  $A_{Film}$  in this regime increases

rapidly with  $R/H$  since  $R/H - 1$  is small. In consequence, the droplet velocity  $U_d$  changes dramatically as  $R/H$  varies around unity.

- Film-dominated regime (Regime F),  $R/H \gg 1$ : In this regime, the droplet velocity is controlled by the lubrication film formed between the droplet and the wall. The film thickness becomes completely independent from the horizontal radius and becomes dependent on  $Ca_f$ . From the simple approximation of  $A_{Film}$  given above, it is shown that the film area increases more gradually for large  $R/H$  and the ratio  $A_{Film}/S_{y=0}$  becomes significant. Similarly to the film thickness,  $U_d$  reaches a plateau value for large  $R/H$ , which decreases with  $Ca_f$ .

The three regimes can also be recognized from the droplet circulation velocities as shown in Fig. 5(d). The  $u$ -velocities at the top (the point with maximum  $y$  on the droplet) and the side of the droplet (the point with minimum  $z$  on the droplet) are denoted as  $U_y$  and  $U_z$ , respectively. The simulation results of Roberts *et al.*<sup>6</sup> and the theoretical results of Hudson<sup>5</sup> are shown for comparison. For  $R/H \ll 1$ , namely in the Poiseuille-dominated regime,  $U_y$  and  $U_z$  vary as parabolic functions with respect to  $R/H$ . The present predictions of  $U_y$  are in good agreement with both the previous numerical results and the theoretical prediction. In the film-dominated regime ( $R/H \gg 1$ ), it is observed that both  $U_y$  and  $U_z$  reach constant values, similar to  $U_d$ . It is also interesting to notice that the relative velocities  $U_y - U_d$  and  $U_z - U_d$  for different  $Ca_f$  seem to overlap.

Another important observation of the present simulation results is that, the droplet velocity in the film-dominated regime is smaller than the average inflow velocity in the Hele–Shaw channel. This low droplet velocity is consistent with the experimental measurements<sup>12,14,16</sup> instead of the Taylor–Saffman prediction<sup>9</sup>. The previous investigations by Saffman and Tanveer<sup>13</sup> and Park *et al.*<sup>14</sup> suggested that the moving contact line within the film and the Magrangoni effect are possible reasons for the discrepancy of the theory with the experimental measurements. Both of these two effects are excluded in the present stimulation (the ambient fluid always wets the channel wall and a constant surface tension is used), however, low droplet velocity  $U_d < U_f$  is still achieved, indicating that there may exist an unexplored mechanism that contributes to low droplet mobility in a Hele–Shaw cell.

It is observed from Fig. 5(a) that when  $R/H$  increases to from 0.5 to 2, the droplet velocity  $U_d$  for  $Ca_f = 9.87 \times 10^{-2}$  decreases from 1.4 to 0.93. In particular, when the lubrication film

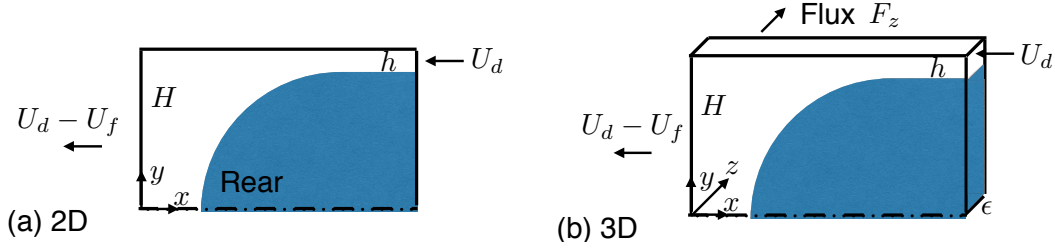


FIG. 6. Schematics of mass fluxes budget for a droplet in (a) 2D and (b) 3D channels.

just starts to form at  $R/H \approx 1$ , the droplet velocity has a sharp decrease. This suggests the lubrication film to be responsible for the low droplet velocity. In the following section, we propose a simple model of mass fluxes balance to illustrate the relation between the lubrication film (and its effect on the 3D flow structure) and the droplet dynamics in a Hele–Shaw cell.

### C. A simple model for droplet dynamics

In the 2D planar (or axisymmetric) geometry the ambient fluid which enters the channel can only move along the flow direction, and thus must push the droplet to move faster than the average inflow velocity to ensure mass conservation. If  $h$  is given the corresponding value of  $U_d$  can be obtained by the balance of mass fluxes<sup>7</sup>. Taking a control volume (of zero thickness) near the rear of the droplet as shown in Fig. 6(a), the mass fluxes are identical to zero on both the  $y$  and  $z$  boundaries and thus the fluxes from the left and right must cancel. Considering a bubble with large  $R/H$  and small  $h/H$ , with a stress-free interface (and thus a constant velocity within the film), the relation between  $h$  and  $U_d$  can be expressed as

$$\frac{U_d - U_f}{U_d} \frac{H}{h} = 1. \quad (10)$$

It is seen that  $U_d > U_f$  for non-zero  $h$ . For small  $h/H$  the excess of droplet velocity is small and the droplet velocity  $U_d$  is close to the average inflow velocity  $U_f$ .

In the 3D analogue, since the ambient fluid can flow around the droplet from the sides (or edge) of the droplet, the mass fluxes balance and the flow pattern become more complex. Similarly to the 2D case we look at a thin layer of small thickness  $\epsilon \ll h$  along the symmetric plane ( $z \in (0, \epsilon)$ ) near the rear of the droplet. As there is zero flux on the symmetric plane  $z = 0$ , the transverse mass flux is only non-zero at the plane  $z = \epsilon$ , normalized by the flux

from the right, *i.e.*,  $U_d h \epsilon$ , which can be expressed as

$$F_{z,rear} = 1 - \frac{U_d - U_f}{U_d} \frac{H}{h}, \quad (11)$$

assuming the variation of  $U_f$  in  $z \in (0, \epsilon)$  is negligible. The transverse flux  $F_{z,rear}$  is not uniformly distributed on the plane  $z = \epsilon$ , instead it is concentrated near the stagnation point at the rear of the droplet. A similar analysis can be performed for the front of the droplet and it can be shown that  $F_{z,rear}$  and  $F_{z,front}$  have the same magnitude but different signs, which creates a circulation around the edge of the droplet.

For a given  $h$ ,  $F_{z,rear}$  is related to  $U_d$  through mass conservation, however the fluxes balance is not sufficient to determine  $U_d$ . This extra spatial degree of freedom of mass flux thus allows a much wider variation of droplet velocity. In contrast to the 2D case, where  $U_d$  is always comparable to  $U_f$ , in the 3D case  $U_d$  has been observed to vary from as low as  $0.1U_f$  to about  $2U_f$ <sup>9,14,16</sup>.

Furthermore the two scenarios of  $U_d > U_f$  and  $U_d < U_f$  correspond to two qualitatively different three-dimensional flow patterns over the droplet. Assuming  $h \ll H$ , it can be shown that  $F_{z,rear} < 0$  when  $U_d > U_f$ . The experiments for “pure” bubbles by Park *et al.*<sup>14</sup> fall in this scenario of high-migration-velocity (HMV). In the droplet reference frame the sweeping motion of the ambient fluid on the edge of the droplet is from the front to the rear. Combined with the fact that the flow on the top of the droplet is always from the front to the rear, this means that the overall flow in the droplet reference frame is in the rear-to-front direction. Therefore a depth-averaged representation (as in the Hele–Shaw equation) is a reasonable approximation of the flow field. This explains why the Taylor–Saffman theory is able to predict the bubble velocity in the HMV scenario.

On the other hand the scenario of low-migration-velocity (LMV), *i.e.*,  $U_d < U_f$  and thus  $F_{z,rear} > 0$ , is very different. The droplets and contaminated bubbles in the experiments of Park *et al.*<sup>14</sup> and Kopf-Sill and Homsy<sup>12</sup> fall in this category. The positive transverse flux near the droplet rear ( $F_{z,rear} > 0$ ) indicates that the fluid actually goes around the droplet from the rear to the front. As a consequence, the relative flows on the top and the side of the droplets are in opposite directions, (which are also illustrated in Fig. 5(d)). A complex interfacial flow sweeping over the droplet is then formed, in which the flow (in the droplet reference frame) first goes from the front to the rear on the top of the droplet then returns from the rear back to the front on the edge of the droplet. (A visualization of this interfacial

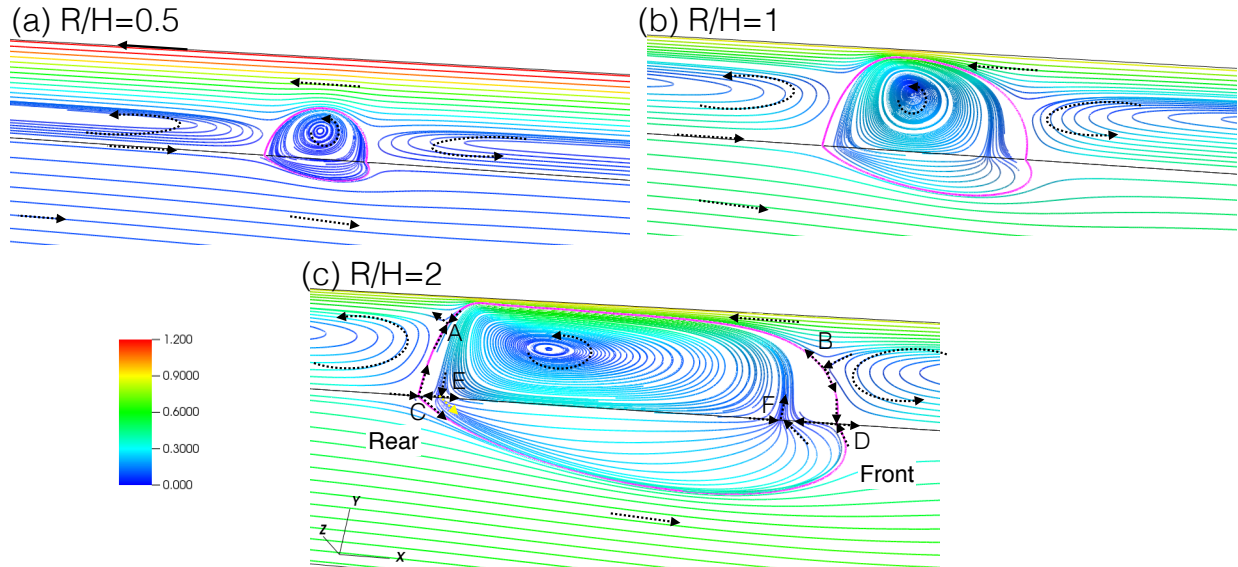


FIG. 7. Streamlines inside and outside of the droplet in the droplet reference frame for  $Ca_f = 9.87 \times 10^{-2}$  and  $R/H = 0.5, 1$  and  $2$ . The color of the streamlines denotes the corresponding relative velocity magnitude. The pink line indicates the droplet interface.

flow is to be presented in Fig. 9.) It is quite obvious that in this case the flow around the droplet is truly three dimensional and thus a depth-averaged 2D Hele–Shaw equation will not be able to represent this scenario correctly. This is the reason why the Taylor–Saffman theory (which is a solution of the depth-averaged equations) cannot be applied.

## D. Effect of three-dimensional flow structure on droplet dynamics

### 1. Streamlines and flow circulation

Since the droplet velocity for large  $R/H$  is lower than the average inflow velocity in the present simulation, the present case belongs to the LMV scenario according to the above analysis. The three-dimensional flow structure inside and outside of the droplet is shown in Fig. 7 for  $Ca_f = 9.87 \times 10^{-2}$  and  $R/H = 0.5, 1$  and  $2$ . The streamlines on the two symmetric planes  $z = 0$  and  $y = 0$  are plotted in the droplet reference frame and colored by the relative velocity magnitude. As the droplet moves faster for smaller droplets the relative velocity magnitude is larger for smaller  $R/H$ . The flow pattern for  $R/H < 1$  here is also consistent with the simulation results of Roberts *et al.*<sup>6</sup>.

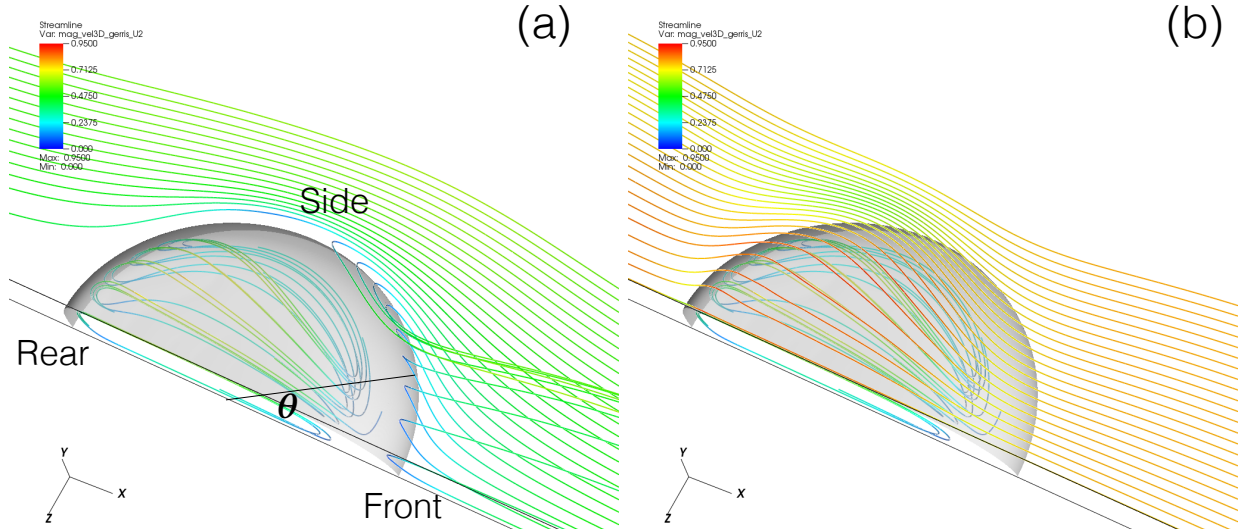


FIG. 8. Streamlines for  $Ca_f = 9.87 \times 10^{-2}$  and  $R/H = 2$  in the droplet reference frame: (a) Internal circulation and external circulation near the front of the droplet. (b) Flow within the film between the droplet and the wall and the internal circulation inside the droplet. The color of the streamlines denotes the magnitude of the relative velocity. The angular coordinate  $\theta$  is defined in the droplet reference frame with the origin located at the center of the horizontal cross-section.

In the vertical plane  $z = 0$  the ambient fluid is moving from right to left at the top ( $y = H$ ) and in a reverse direction at the center plane ( $y = 0$ ). As a result two external circulations develop outside of the droplet, similar to the 2D analogue shown in Fig. 3(a). The external flow will also drive internal circulation inside the droplet. Similarly to the 2D case, six stagnation points (A, B, C, D on the droplet interface and E, F inside the droplet) can be seen, however the stagnation flow around these points becomes three dimensional. For example in the 2D case, the flow reaches the rear stagnation point C and can only turn toward point A and then turn again to the left and leave the domain, forming a counter-clockwise external circulation, see Fig. 3(a). In 3D the fluid has an extra degree of freedom to go in the  $z$  direction around the droplet toward the stagnation point D, see the streamlines on the  $x$ - $z$  plane in Fig. 7(c). This transverse fluid motion near the stagnation point C is characterized by  $F_{z, rear}$  in the model presented in section IV C. Due to the 3D flow structure, the minor internal circulations (A-E-C-A and B-D-F-B) in the 2D case are invisible here.

The 3D flow structure significantly affects the external and internal circulating flow. As shown in Fig. 8(a), the 3D streamlines inside and outside of the droplet become very

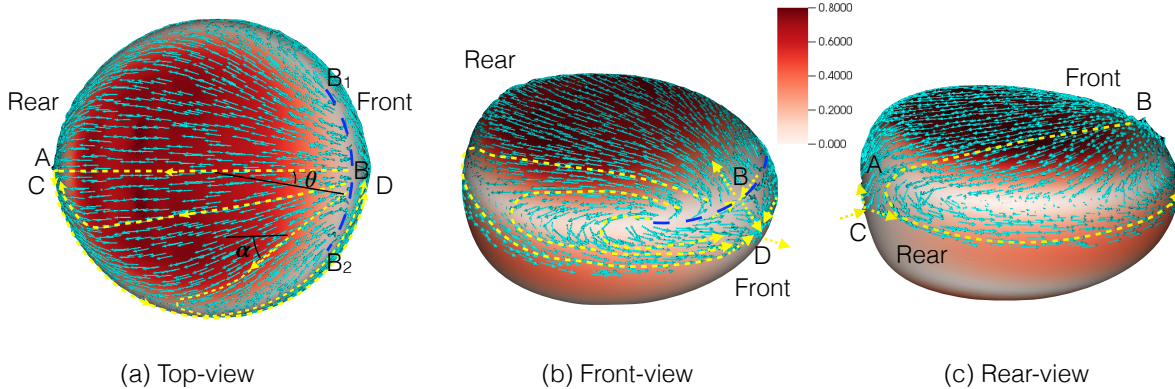


FIG. 9. (a) Top- (b) front- and (c) rear-views of relative velocity in the droplet reference frame  $\{u - U_d, v, w\}$  on the droplet interface for  $Ca_f = 9.87 \times 10^{-2}$  and  $R/H = 0.5, 1$  and  $2$ . The color denotes the magnitude of the relative velocity.

complicated and are very dependent on the angular coordinate  $\theta$ . (Here  $\theta$  is defined as the angle between the normal to the interface in the  $x-z$  plane and the  $x$  axis.) For  $\theta = 0$  the circulation is perfectly aligned with the symmetric  $x-y$  plane. As  $\theta$  increases the external circulation is twisted in a complex manner while trying to adjust to the droplet shape. At about  $\theta \approx 60$  degrees the streamlines are almost tangential to the droplet interface. Therefore, in contrast with the typical quasi-2D flows in a Hele–Shaw cell, droplet migration in the Hele–Shaw microchannel generates a fully 3D flow.

## 2. Velocity field on the droplet interface

The vectors of the droplet velocity in the droplet reference frame are shown in Fig. 9. The color of the interface indicates the relative velocity magnitude. Regions with white color indicate zero velocity, *i.e.*, stagnation regions on the droplet interface. The four stagnation points (A, B, C, D) on the droplet interface and 3D stagnation flows in the vicinity can be clearly seen.

Driven by the flow within the film, the interfacial flow on the top of the droplet moves to the left; while the flow on the edge near the center plane  $y = 0$  moves in the opposite direction. An interesting and complex interfacial flow is then formed on the droplet interface, which is highlighted with yellow dashed lines in Fig. 9. At first the flow starts from the vicinity of stagnation point B (indicated by the blue dashed line  $B_1B_2$ ), and goes toward

the rear. It is seen that the velocity vectors on the top interface are not parallel to the  $x$  axis, instead they turn toward the side of the droplet. The angle between the top interfacial flow and the  $-x$  axis is denoted by  $\alpha$  here, and it can be seen that  $\alpha$  varies significantly with the angle  $\theta$  of the relative flow near the wall (in the droplet reference frame). For  $\theta = 0$ ,  $\alpha = 0$ , but then  $\alpha$  increases significantly with  $\theta$  up to about 45 degrees. Then top interfacial flow is observed to curve back toward the center plane ( $z = 0$ ) before reaching stagnation point A. After reaching point A the flow reverses its direction and moves toward the front stagnation point D along the edge of the droplet. For the top interfacial flow leaving from  $B_1B_2$  with a large  $\theta$ , the flow may not get a chance to turn back to stagnation point A before returning to the front. As a result a ring of zero interfacial velocity (the region in white color) is formed on the edge of the top where the interfacial flow reverses direction. Near the rear of the droplet the expected up-going interfacial flow from stagnation points C to A is not seen due to the strong interfacial flow along the edge. The stagnation flows near C and A seem to merge, forming a stagnation area at the droplet rear.

Furthermore the streamlines in Fig. 8(b) show that the flow within the lubrication film is influenced by the complex interfacial flow on the droplet interface. When the flow passes through the top of the droplet the streamlines off the center plane  $z = 0$  also first turn toward the side and then return back to the center.

As shown above the flow within the Hele–Shaw channel for the Low-migration-velocity (LMV) scenario is much more complicated than the high-migration-velocity (HMV) case, according to the characterization given in section IV C. In particular the streamwise component of the interfacial flow velocity reverse sign. Therefore a depth-averaged 2D Hele–Shaw equation that is valid for the HMV case is not able to capture the flow structure of the LMV case. As the Taylor–Saffman prediction of the droplet/bubble velocity is a solution of the depth-averaged Hele–Shaw equation, it is not surprising that it does not match the experimental and numerical results of the LMV scenario.

## E. Configuration and dynamics of the lubrication film

Recent experiments by Huerre *et al.*<sup>16</sup> have shown that the droplet velocity decreases with the film thickness. The reduction of the film thickness may introduce a strong shear on the droplet interface, which in turn slows down the motion of the bubble/droplet. To

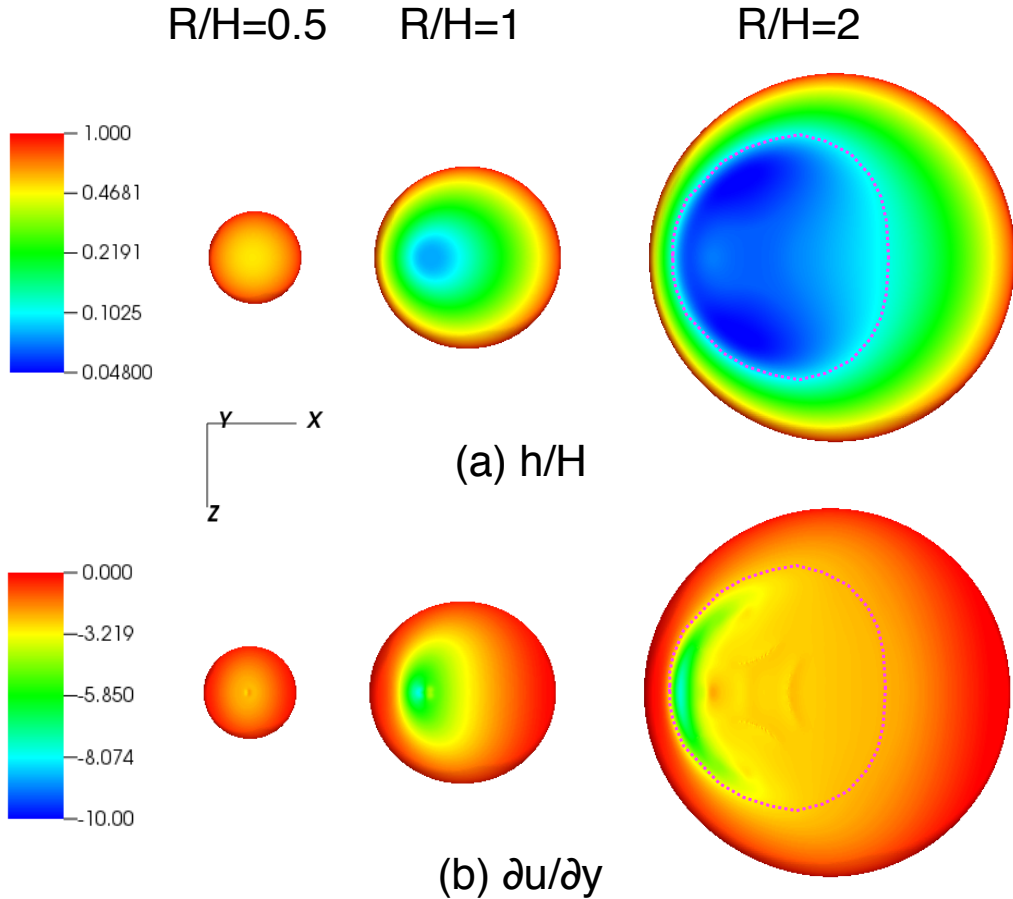


FIG. 10. (a) Thickness (height) of the film (gap) between the interface and the wall  $h/H$  and (b) shear  $\partial u/\partial y$  on the interface for  $Ca_f = 9.87 \times 10^{-2}$  and  $R/H = 0.5, 1$  and  $2$ . The film for  $R/H = 2$  is highlighted by pink dotted lines.

better understand the effect of the lubrication film on the droplet dynamics, the thickness of the lubrication film and the shear on the droplet top interface are shown in Fig. 10 for  $Ca_f = 9.87 \times 10^{-2}$  and  $R/H = 0.5, 1$  and  $2$ .

As  $R/H$  is small the gap between the droplet and the wall is large and thus strictly speaking there exists no film, the term is retained only for convenience. When  $R/H$  is larger or comparable to unity a thin lubrication film with small thickness can be clearly seen. In particular for  $R/H = 2$  the film area (highlighted by the pink dotted line) becomes quite large compared to the cross-section of the droplet at the  $y = 0$  plane. Instead of being centered, the lubrication film is shifted toward the rear (see Fig. 9). The overall film exhibits a “peach” shape.

Values of the shear  $\partial u/\partial y$  on the droplet interface are shown in Fig. 10(b). When  $R/H$  is small the droplet is away from the top wall and the shear on the top of the droplet is indeed quite small. The shear increases dramatically as  $R/H$  becomes comparable or larger than unity. For  $R/H = 2$  the large negative shear is located near the rear. The region of high shear has a croissant shape, and minimum shear rate reaches about  $(\partial u/\partial y)_{\min} = -8$  (in dimensionless unit), the magnitude of which is more than two times larger than the minimum shear in the ambient 2D Poiseuille flow, *i.e.*  $(\partial u/\partial y)_{\min, \text{Poiseuille}} = -3$ . It is obvious that the strong shear stress within the film contributes to the significant decrease of the droplet velocity as  $R/H \gtrsim 1$  as shown in Fig. 5(b).

## F. Effect of capillary number on film and droplet dynamics

As mentioned at the beginning of this section, the capillary numbers considered in the 3D simulations are larger than that in experiments. To justify that the simulation results presented above still at least qualitatively reflect the correct flow physics of droplet migration in a Hele–Shaw microchannel, the capillary number is varied to investigate its effect on the results. From Fig. 5(b), it can be seen that the droplet changes little for small  $R/H$  as  $\text{Ca}_f$  varies from  $9.87 \times 10^{-2}$  to  $6.17 \times 10^{-3}$ , indicating that the effect of surface tension is small on droplets with small  $R/H$ . Therefore, though smaller capillary numbers are used, the surface tension is still sufficient to keep the droplet spherical and the droplet velocity is mainly controlled by the viscous stress. The droplet velocity obtained in simulations for  $\text{Ca}_f = 9.87 \times 10^{-2}$ , which is two order of magnitude larger than that in experiments, still agrees quite well with the experimental and theoretical results. On the other hand, as  $R/H \gtrsim 1$ , the effect of the capillary number on the droplet velocity becomes much stronger. As shown in Fig. 5(b) and (c), the droplet velocity and film thickness decrease by about 12.2% and 53.3% for  $R/H = 2$ , when  $\text{Ca}$  decreases from  $9.87 \times 10^{-2}$  to  $2.47 \times 10^{-2}$ .

The film thickness and shear on the droplet interface for  $\text{Ca}_f = 2.47 \times 10^{-2}$  and  $R/H = 0.5, 1$  and  $2$  are shown in Fig. 11. The surface tension here is four times that in Fig. 10 while the other parameters remain the same. (Correspondingly  $\text{Ca}_f$  in Fig. 11 is a quarter of that in Fig. 10.) The legends for film thickness in Figs. 10(a) and 11(a) are different to reflect the fact that the film becomes significantly thinner as surface tension increases. The minimum film thickness for  $\text{Ca}_f = 2.47 \times 10^{-2}$  is about  $h_{\min} = 0.015H$  while for  $\text{Ca}_f = 9.87 \times 10^{-2}$ ,

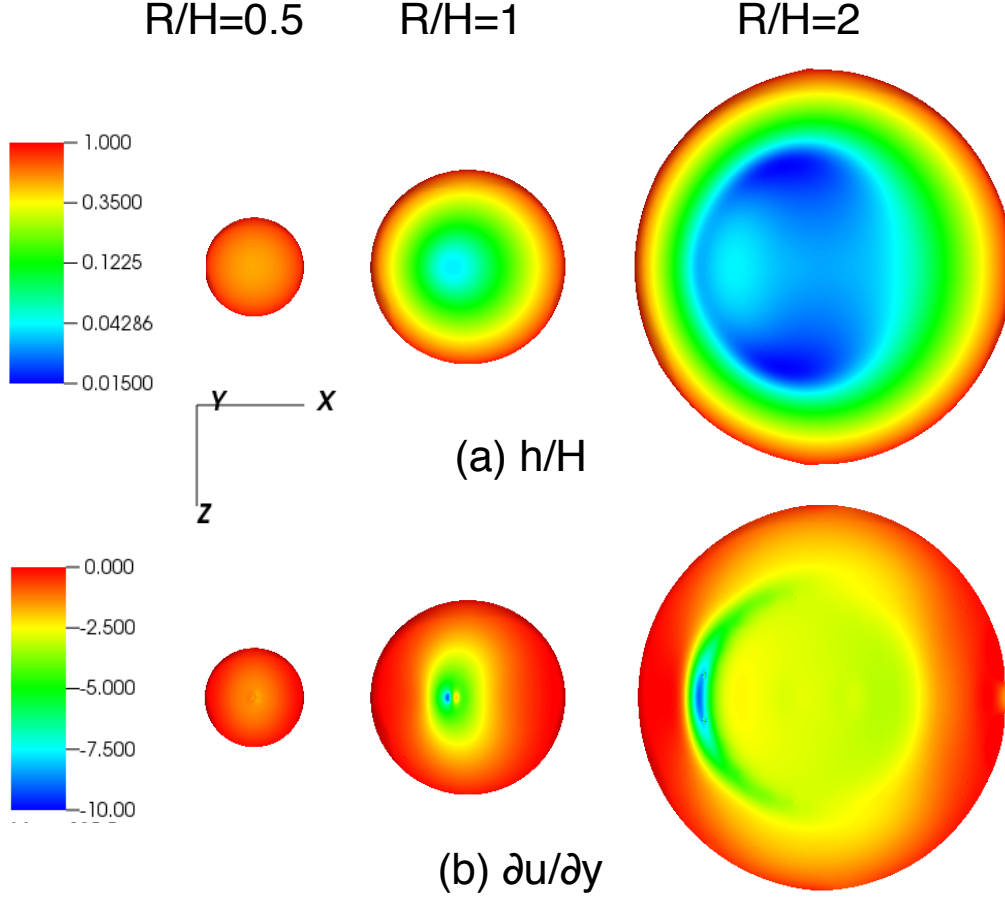


FIG. 11. (a) Thickness of the gap between the interface and the wall  $h/H$  and (b) shear  $\partial u/\partial y$  on the interface for  $Ca_f = 2.47 \times 10^{-2}$  and  $R/H = 0.5, 1$  and  $2$ .

$h_{\min} = 0.048H$ . When  $R/H$  is small there is no difference in the gap thickness. For large  $R/H$ , when  $Ca_f$  decreases, the lubrication film still shifts to the rear, however the shift becomes smaller and the droplet shape becomes more symmetric with regard to the  $y$ - $z$  plane. Furthermore the overall “peach” shape of the film remains and the smallest film thickness for  $R/H = 2$  is obtained at the two sides of the film.

When  $Ca_f$  decreases the general distribution of the shear rate within the film is similar. The high shear region still holds a croissant shape. The minimum shear near the rear decreases to about  $-10$  which is about 25% larger than that for  $Ca_f = 9.87 \times 10^{-2}$  in magnitude. This indicates that the decreases of  $Ca_f$  and  $h$  introduce a stronger shear drag on the droplet and reduce the droplet migration velocity.

The film thickness as a function of  $Ca$  is plotted in Fig. 12(a), where  $Ca = \mu_f U_d/\sigma$  is

the capillary number based on the droplet velocity  $U_d$ . The 2D theory, *i.e.*, Eq. (8) is also plotted for comparison. It is seen that  $h/H$  in the 3D case is much smaller than in the 2D case. For  $Ca = 9.87 \times 10^{-2}$ ,  $h$  in 3D is an order of magnitude smaller than in 2D, as already visualized in Figs. 3 and 7. Due to the effect of the 3D flow, the droplet moves much slower in 3D than in 2D for the same capillary number. As a consequence the viscous stress that overcomes the surface tension decreases, which in turn reduces the film thickness. The film thickness variation with capillary number also seems to follow a power law but the power coefficient is about 0.4 instead of 2/3 as in 2D.

The droplet velocity  $U_d$  as a function of  $Ca_f$  is shown in Fig. 12(b). Here the capillary number based on the average inflow velocity is used following previous works<sup>12,14</sup>. In general it can be observed that  $U_d$  decreases with  $Ca_f$ . The range of  $Ca_f$  considered in the present simulation is an order of magnitude larger than the experimental value. It is hard to tell if the simulation results would match with the experimental measurements<sup>6</sup> if the same  $Ca_f$  is used. Nevertheless it seems like the computed  $U_d$  approach the experimental value as  $Ca_f$  decreases.

As discussed previously the mass fluxes balance in 3D is substantially different from 2D. In the 2D case it is known that  $(U_d - U_f)/U_f = h/H$  (for  $h/H \ll 1$ ), however, in 3D, it can be seen from Fig. 12(c) that  $(U_d - U_f)/U_f$  becomes negative.  $U_d$  decreases with  $h/H$  as in 2D, but the decrease is non-linear and follow a much faster decay of  $(h/H)^{1/4}$  as indicated in Fig. 12(c).

The simple model of transverse flux near the rear of the droplet (Eq. (11)) can serve as a measure of the three-dimensional “strength” of the flow. The variation of  $F_{z,rear}$  is plotted as a function of the film thickness in Fig. 12(d). When  $h$  decreases it is observed that  $F_{z,rear}$  increases rapidly. As the film becomes thinner, the drag caused by the lubrication film becomes stronger and it is more difficult for the ambient fluid to push the droplet forward. As a result the ambient fluid entering the channel tends to go around the droplet from the transverse edge instead of pushing the droplet. Therefore it is quite clear that both the 3D flow effect and the lubrication film contribute to the low mobility of the droplet.

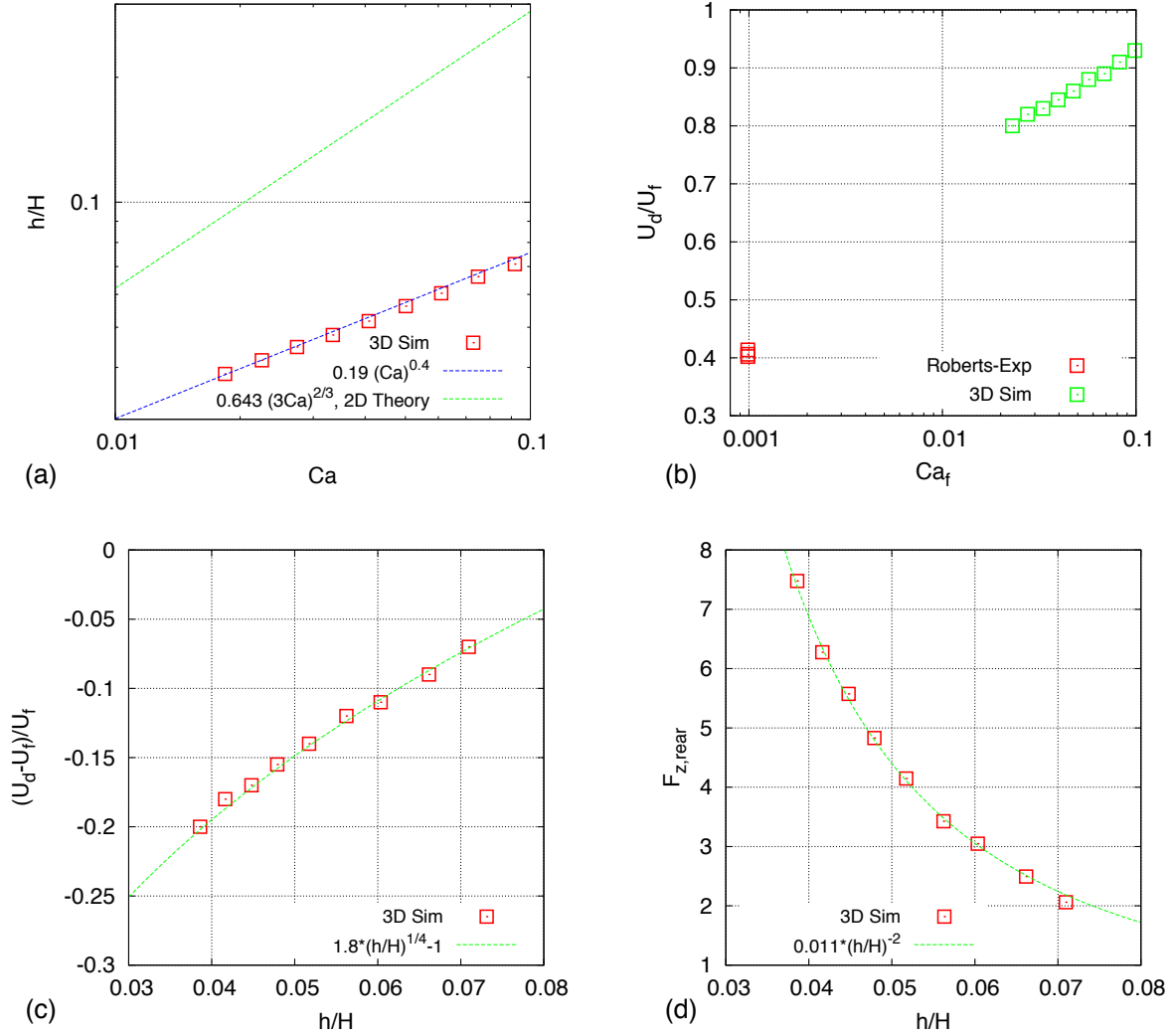


FIG. 12. (a) The film thickness and (b) droplet velocity as functions of the capillary number. (c) Excess of droplet velocity compared to the average inflow velocity and (d) Normalized transverse flux near the rear of the droplet as a function of the film thickness.

## G. Discussions of computational costs

The present simulations are performed on 8 to 24 processors for 3 to 25 days depending on cases. The adaptive meshes used for  $Ca_f = 9.87 \times 10^{-2}$  and  $2.47 \times 10^{-2}$  and  $R/H = 2$  are shown in Fig. 13. The main constraint on the computational efficiency is from the small time step which is in turn restricted by the surface tension (or capillary number), see Eq. (6). When surface tension increases four times, the time step is divided by two and namely

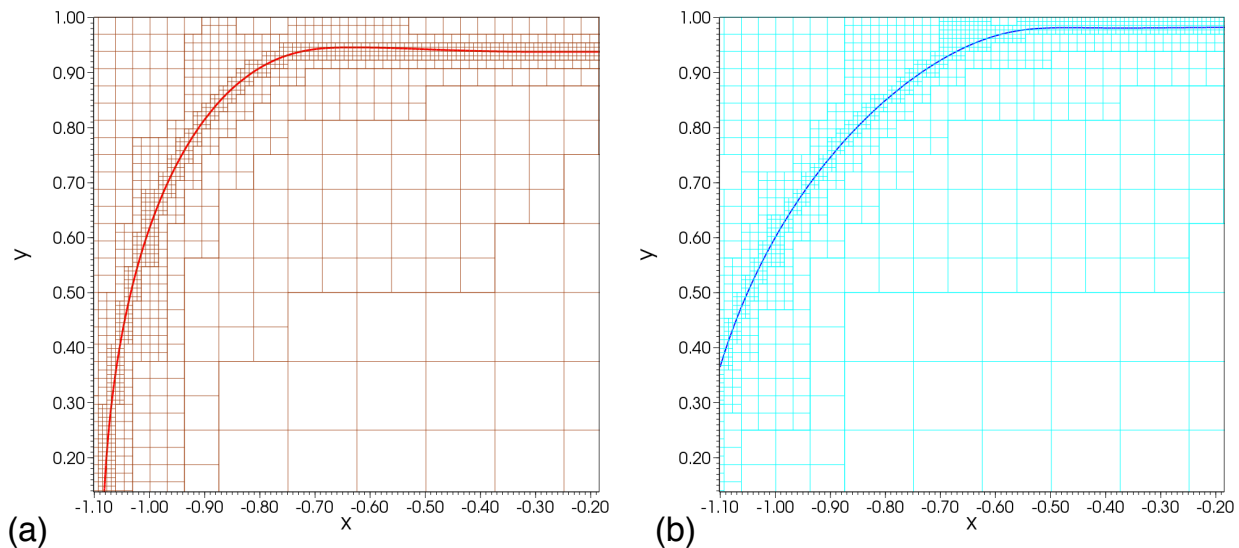


FIG. 13. Mesh and interface on the plane  $z = 0$  for  $R/H = 2$  and (a)  $Ca_f = 9.87 \times 10^{-2}$  and (b)  $Ca_f = 2.47 \times 10^{-2}$ .

the computational time doubles assuming the mesh is unchanged. However, as indicated in Fig. 13(b) that if  $Ca_f$  is further decreased, the minimum mesh size in the adaptive mesh, *i.e.*,  $\Delta_{min} = H/128$ , will not be sufficient and thus must be refined. Therefore, even with an adaptive mesh, it is too expensive to simulate droplets at capillary number comparable to experiments for large  $R/H$ . To perform 3D direct simulation of droplets at low capillary number, novel numerical schemes to compute the surface tension are required. If the surface tension term in Eq. (1) can be treated in an implicit manner similar to what is done for the viscous term in Stokes flow (at low Reynolds number), then the time-step restriction due to the explicit integration of the surface tension term can be lifted (the authors are not aware of this type of scheme in the literature). Nevertheless the development of an implicit treatment of surface tension is out of the scope of the present paper and will be relegated to future work.

## V. CONCLUSIONS

The migration of a droplet in a Hele–Shaw microchannel has been investigated by 3D direct numerical simulations. We focused on the regime at low capillary number where the droplet remains circular in the horizontal plane. Parametric studies were performed by vary-

ing the droplet horizontal radius and the capillary number, and particular attention was paid to the effect of the lubrication film on the droplet dynamics. For droplets with an horizontal radius  $R$  larger than the half-height of the channel  $H$ , the droplet overfills the channel and a lubrication film is formed between the droplet and the wall. The ratio  $R/H$  has a significant impact on the droplet velocity and controls three regimes: the Poiseuille-dominated regime, the film-dominated regime, and the transition regime. Excluding moving contact lines and the Marangoni effects, which were proposed as potential mechanisms to explain the low droplet velocity and the discrepancy of the experimental measurements with the Taylor–Saffman theory<sup>13,14</sup>, the droplet velocity (for large  $R/H$ ) in the present simulations is observed to be lower than the average inflow velocity, consistent with experimental observations and in disagreement with the Taylor–Saffman prediction. The strong shear induced by the lubrication film and the three-dimensional flow structure seem to both contribute to the low mobility of the droplet. In this low-migration-velocity scenario, the interfacial flow on the droplet become more complex and is fully three dimensional. As a result the Hele–Shaw equation, which is a depth-averaged 2D approximation, and the Taylor–Saffman solution are not valid for this case. As the shear induced by the lubrication film seems to have a strong influence on the droplet dynamics, the viscosity ratio can be an important parameter for the present problem, and we intend to investigate its influence in future work.

## ACKNOWLEDGEMENTS

This project has been supported by the the ANR TRAM project (ANR-13-BS09-0011). The simulations of this paper are conducted on the our lab cluster, and the CINES Occigen machine for which we thankfully acknowledge grant x20152b7325 from GENCI.

## REFERENCES

- <sup>1</sup>H. A. Stone, A. D. Stroock, and A. Ajdari, “Engineering flows in small devices: microfluidics toward a lab-on-a-chip,” *Annu. Rev. Fluid Mech.* **36**, 381–411 (2004).
- <sup>2</sup>R. B. Fair, “Digital microfluidics: is a true lab-on-a-chip possible?” *Microfluid Nanofluid* **3**, 245–281 (2007).

- <sup>3</sup>S.-Y. Teh, R. Lin, L.-H. Hung, and A. P. Lee, “Droplet microfluidics,” *Lab Chip* **8**, 198–220 (2008).
- <sup>4</sup>A. Nadim and H. A. Stone, “The motion of small particles and droplets in quadratic flows,” *Stud. Appl. Math.* **85**, 53–73 (1991).
- <sup>5</sup>S. D. Hudson, “Poiseuille flow and drop circulation in microchannels,” *Rheol. Acta.* **49**, 237–243 (2010).
- <sup>6</sup>C. C. Roberts, S. A. Roberts, M. B. Nemer, and R. R. Rao, “Circulation within confined droplets in Hele–Shaw channels,” *Phys. Fluids* **26**, 032105 (2014).
- <sup>7</sup>F. P. Bretherton, “The motion of long bubbles in tubes,” *J. Fluid Mech.* **10**, 166–188 (1961).
- <sup>8</sup>S. R. Hodges, O. E. Jensen, and J. M. Rallison, “The motion of a viscous drop through a cylindrical tube,” *J. Fluid Mech.* **501**, 279–301 (2004).
- <sup>9</sup>G. I. Taylor and P. F. Saffman, “A note on the motion of bubbles in a Hele–Shaw cell and porous medium,” *Quart. J. Mech. Appl. Math.* **12**, 265–279 (1959).
- <sup>10</sup>S. Tanveer, “The effect of surface tension on the shape of a Hele–Shaw cell bubble,” *Phys. Fluids* **29**, 3537–3548 (1986).
- <sup>11</sup>S. Tanveer, “New solutions for steady bubbles in a Hele–Shaw cell,” *Phys. Fluids* **30**, 651–658 (1987).
- <sup>12</sup>A. R. Kopf-Sill and G. M. Homsy, “Bubble motion in a Hele–Shaw cell,” *Phys. Fluids* **31**, 18–26 (1988).
- <sup>13</sup>P. F. Saffman and S. Tanveer, “Prediction of bubble velocity in a Hele–Shaw cell: Thin film and contact angle effects,” *Phys. Fluids* **1**, 219–223 (1989).
- <sup>14</sup>C.-W. Park, S. R. K. Maruvada, and D.-Y. Yoon, “The influence of surfactant on the bubble motion in Hele–Shaw cells,” *Phys. Fluids* **6**, 3267–3275 (1994).
- <sup>15</sup>S. R. K. Maruvada and C.-W. Park, “Retarded motion of bubbles in Hele–Shaw cells,” *Phys. Fluids* **8**, 3229–3233 (1996).
- <sup>16</sup>A. Huerre, O. Theodoly, A. M. Leshansky, M.-P. Valignat, I. Cantat, and M.-C. Jullien, “Droplets in microchannels: Dynamical properties of the lubrication film,” *Phys. Rev. Lett.* **115**, 064501 (2015).
- <sup>17</sup>S. Afkhami, A. M. Leshansky, and Y. Renardy, “Numerical investigation of elongated drops in a microfluidic T-junction,” *Phys. Fluids* **23**, 022002 (2011).

- <sup>18</sup>A. Bedram and A. Moosavi, “Breakup of droplets in micro and nanofluidic T-Junctions,” *J. Appl. Fluid Mech.* **6**, 81–86 (2013).
- <sup>19</sup>D. A. Hoang, V. van Steijn, L. M. Portela, M. T. Kreutzer, and C. R. Kleijn, “Benchmark numerical simulations of segmented two-phase flows in microchannels using the volume of fluid method,” *Comput. Fluids* **86**, 28–36 (2013).
- <sup>20</sup>D. A. Hoang, L. M. Portela, C. R. Kleijn, M. T. Kreutzer, and V. van Steijn, “Dynamics of droplet breakup in a T-junction,” *J. Fluid Mech.* **717**, R4 (2013).
- <sup>21</sup>S. Popinet, “Gerris: a tree-based adaptive solver for the incompressible euler equations in complex geometries,” *J. Comput. Phys.* **190**, 572–600 (2003).
- <sup>22</sup>S. Popinet, “An accurate adaptive solver for surface-tension-driven interfacial flows,” *J. Comput. Phys.* **228**, 5838–5866 (2009).
- <sup>23</sup>R. Scardovelli and S. Zaleski, “Direct numerical simulation of free-surface and interfacial flow,” *Annu. Rev. Fluid Mech.* **31**, 567–603 (1999).
- <sup>24</sup>G. Tryggvason, R. Scardovelli, and S. Zaleski, *Direct numerical simulations of gas-liquid multiphase flows* (Cambridge University Press, 2011).
- <sup>25</sup>C. N. Baroud, F. Gallaire, and R. Dangla, “Dynamics of microfluidic droplets,” *Lab Chip.* **10**, 2032–2045 (2010).